



In₂S₃/F-Fe₂O₃ type-II heterojunction bonded by interfacial S-O for enhanced charge separation and transport in photoelectrochemical water oxidation

Huan Chai^a, Lili Gao^a, Peng Wang^a, Feng Li^b, Guowen Hu^a, Jun Jin^{a,*}

^a State Key Laboratory of Applied Organic Chemistry (SKLAOC), The Key Laboratory of Catalytic Engineering of Gansu Province, Key Laboratory of Advanced Catalysis of Gansu Province, College of Chemistry and Chemical Engineering, Lanzhou University, Lanzhou, Gansu 730000, China

^b State Key Laboratory of High-Efficiency Utilization of Coal and Green Chemical Engineering, College of Chemistry and Chemical Engineering, Ningxia University, Yinchuan, Ningxia 750021, China

ARTICLE INFO

Keywords:

α -Fe₂O₃ photoanode
Indium sulfide
Heterojunction
S-O bond
Photoelectrochemical water oxidation

ABSTRACT

The application of hematite(α -Fe₂O₃)-based photoanodes in photoelectrochemical (PEC) water oxidation has been hampered by disgusting charge recombination and difficult carrier migration. Herein, we modified indium sulfide (In₂S₃) nanoparticles on the surface of fluorine-doped α -Fe₂O₃ (F-Fe₂O₃) nanorods. The In₂S₃/F-Fe₂O₃ heterostructure bonded by S-O chemical bond shows a superior photocurrent density of 2.21 mA cm⁻² at 1.23 V versus reversible hydrogen electrode (around 3.45 times higher than that of pristine α -Fe₂O₃). In-depth investigations show that In₂S₃/F-Fe₂O₃ has significantly increased donor density and decreased charge transfer resistance. Simultaneously, In₂S₃ decorated with S-O bond could reduce the surface defect states. Further studies of energy band location reveal the formation of type-II heterojunction between In₂S₃ and F-Fe₂O₃. The unique heterostructure provides a powerful driving force for charge separation and transport, resulting in satisfactory bulk phase and surface separation efficiency. This work provides ideas for the design and study of multicomponent photoanodes.

1. Introduction

The global energy crisis had an unsettling impact on the progress and development of society. The increasing exhaustion of non-renewable resources represented by fossil fuels promotes people's thirst for renewable clean energy. Photoelectrochemical (PEC) water splitting, which converts solar energy into hydrogen energy, has great potential to meet people's energy needs [1–4]. With the intense exploration and research of PEC cell, the photocathode (especially the p-type silicon base) has made great progress, while the photoanode still needs great efforts to improve PEC performance [5–7].

Because hematite (α -Fe₂O₃) not only has abundant natural reserves and ecological friendliness, but also has excellent stability and narrow band gap (1.9–2.2 eV), it has become one of the most promising and potential candidate photoanode materials [8–11]. However, due to the disadvantages of poor conductivity, short photogenerated carrier lifetime ($\sim 10^{-12}$ s) and short hole migration distance (~ 2 –4 nm) of α -Fe₂O₃, the photocurrent density of α -Fe₂O₃-based photoanode at 1.23

V versus reversible hydrogen electrode (RHE) is still far from its theoretical value (12.6 mA cm⁻² at 1.23 V_{RHE}) [3,10,12,13]. In the past, researchers had focused heavily on key aspects of photoanode materials such as photon absorption, stability, surface reaction dynamics, charge separation and transport [14–19]. Fortunately, α -Fe₂O₃ has excellent and satisfactory stability compared with BiVO₄ and ZnO; Compared with TiO₂, α -Fe₂O₃ has a narrower band gap and a larger light absorption range. In addition, cobalt phosphate [20,21], Au [22], Ru [23], Ir [24] and Layered Double Hydroxide (LDH) [25,26] were used as co-catalysts to boost dilatory oxygen evolution reaction (OER) kinetics [27]. However, their associated high price, low natural reserves, reliability and other problems greatly limit their wide application for PEC cell in the future. At the same time, they do not contribute much to the inherent low conductivity and low charge separation efficiency of α -Fe₂O₃. Therefore, it is necessary to focus on the conductivity, charge separation and transfer of α -Fe₂O₃ to improve its PEC performance.

Doping is considered to be one of the most common and effective methods to improve the conductivity of α -Fe₂O₃ [28,29]. Sn [30,31], Ti

* Corresponding author.

E-mail address: jinjun@lzu.edu.cn (J. Jin).

<https://doi.org/10.1016/j.apcatb.2021.121011>

Received 17 September 2021; Received in revised form 23 November 2021; Accepted 10 December 2021

Available online 15 December 2021

0926-3373/© 2021 Elsevier B.V. All rights reserved.

[32,33], Ge [34], Si [35] and other dopants have been proved to effectively improve the electron mobility of α -Fe₂O₃. Among them, fluorine (F), as a nonmetallic n-type dopant, can greatly increase the carrier concentration of α -Fe₂O₃, thus effectively improving its electrical conductivity [36–38]. In addition, the formation of heterojunction between α -Fe₂O₃ and introduced foreign semiconductor materials is also a resultful measure to significantly improve charge separation [39]. For example, Cu₂S/Fe₂O₃ [40], CuO/Fe₂O₃ [41], NiO/P-Fe₂O₃ [42], In₂O₃/Ti-Fe₂O₃ [43], TiO₂/Fe₂O₃ [44], MoS₂/W-Fe₂O₃ [45], CoO_x/La-FeO₃/Fe₂O₃ [46], CoPi/CaFe₂O₄/Fe₂O₃ [47], NiFeO_x/FeNbO₄/Fe₂O₃ [48] and other heterojunctions have been demonstrated to be used for enhanced PEC water oxidation. In particular, it is worth mentioning that indium sulfide (In₂S₃) has a band gap (2.0–2.2 eV) similar to that of α -Fe₂O₃, and its heterojunction with TiO₂ or WO₃ has been verified to be suitable for PEC water oxidation [49,50]. Consequently, In₂S₃ may be an appropriate semiconductor material to form heterojunction with α -Fe₂O₃ for enhanced PEC water oxidation.

Herein, we modified In₂S₃ nanoparticles (NPs) on the surface of F-doped α -Fe₂O₃ (F-Fe₂O₃) nanorods (NRs) array by hydrothermal and subsequent thermal annealing methods. The existence of S-O bond between F-Fe₂O₃ and In₂S₃ interface was confirmed, and it is very important for PEC properties of composite photoanode. A series of detailed characterizations clearly illustrate the band positions of F-Fe₂O₃ and In₂S₃ and the formation of type-II heterojunctions. Complete PEC tests and analyses show that F doping and heterogeneous In₂S₃ modification can significantly reduce the charge transfer resistance, effectively inhibit the recombination of electron-hole pairs, promote charge separation and prolong the carrier lifetime. Ultimately, without the aid of any cocatalyst, the In₂S₃/F-Fe₂O₃ photoanode exhibits a high photocurrent density of 2.21 mA cm⁻² at 1.23 V_{RHE} and incident photon-to-current conversion efficiency (IPCE) of 35% at 350 nm, which are 3.45 and 3.89 times higher than those of the pristine α -Fe₂O₃, respectively. By finding heterostructure materials suitable for α -Fe₂O₃-based photoanode, the PEC performance is improved, which provides a reference strategy for the development of multicomponent photoanode materials.

2. Experimental section

2.1. Materials

FeCl₃·6 H₂O, urea and KOH were purchased from Aladdin Industrial Corporation. Na₂SO₃, ethyl alcohol and acetone were obtained from Sinopharm Chemical Reagent Co., Ltd. InCl₃·4 H₂O (>99.99%), NH₄F and thioacetamide (>98%, CH₃CSNH₂) were acquired from Shanghai Macklin Biochemical Co., Ltd. F-doped tin oxide (FTO, <15 Ω /sq) conductive glasses were chosen from Nippon Sheet Glass Co., Ltd. Before the experiment, all FTO substrates (pre-cut as: 1 cm × 3 cm) were ultrasonically washed for 15 min with cleaning agent, deionized (DI) water, acetone, ethanol and DI water in a particular sequence. These reagents are analytical grade reagents and can be used without further purification.

2.2. Fabrication of photoanodes

α -Fe₂O₃ and F-Fe₂O₃ (marked as FH) NRs array photoanodes were synthesized according to our previous work [38,51]. On that basis, In₂S₃/F-Fe₂O₃ photoanode was prepared by hydrothermal reaction and subsequent annealing process. To be specific, the F-Fe₂O₃ NRs array on FTO substrate in a conductive face down manner was placed in a Teflon lining containing 2.012 mM InCl₃·4 H₂O, 3.145 mM CH₃CSNH₂ and 10 ml of DI water, then quickly transferred to a stainless steel high-pressure reactor for sealing and heating at 150 °C for 90 min. After the reaction was completed, the sample was cooled to room temperature and then washed with DI water and dried by nitrogen flow. The In₂S₃/F-Fe₂O₃ (marked as IFH) photoanode was then annealed in argon atmosphere for

10 min at 350 °C at a heating rate of 3 °C/s (the IFH in the following is the annealed In₂S₃/F-Fe₂O₃ photoanode by default).

For comparison, the unannealed In₂S₃/F-Fe₂O₃ (marked as unIFH) photoanode was prepared only by the above hydrothermal reaction. In addition, In₂S₃ powder was also prepared. Specific as follows, after hydrothermal reaction, In₂S₃ turbid liquid was centrifuged at 10,000 rpm for 5 min to obtain In₂S₃ precipitation, and the supernatant liquor was poured out, then washed with deionized water for several times, and then dried at 60 °C for 12 h. After that, the dried product was gently ground to get In₂S₃ powder.

2.3. Characterizations

All photoanodes were characterized by scanning electron microscopy (SEM; type of Hitachi S-4800), transmission electron microscopy (TEM), high-resolution TEM (HRTEM; Tecnai G2Tf20 transmission electron microscope operated at 200 kV), energy-dispersive X-ray spectroscopy (EDS) elemental mapping (investigated by using an annular darkfield detector under TEM), X-ray diffraction spectra (XRD; conducted on a Rigaku D/max-2400 diffractometer with the X-ray source of Cu K α radiation and data were collected in Bragg-Brentano mode with a scan rate of 0.2° s⁻¹ in the range of 10°–90°), X-ray photoelectron spectroscopy (XPS; operated on a Kratos Axis Nova X-ray photoelectron spectrometer with a monochromatic Al K α X-ray source, operating at 15 kV and 10 mA, calibration was performed with the binding energy of 284.6 eV of C 1 s). The light absorption abilities and band gaps of all samples were measured by UV–vis absorption spectra (Hitachi U-4000) with BaSO₄ as the reference. The work functions and valence bands were determined by Ultraviolet photoelectron spectroscopy (UPS; conducted on a Kratos Axis Ultra DLD, He I photon source of 21.2 eV).

3. Results and discussion

3.1. Structure characterizations

The schematic diagram of the fabrication process for IFH photoanode is shown in Scheme S1. The prepared FH was heated in an aqueous solution of InCl₃ and CH₃CSNH₂ at 150 °C for 90 min. After cooling to room temperature, the sample was washed with DI water and dried by N₂ flow, and then annealed in argon at 350 °C for 10 min to obtain IFH photoanode.

In order to study the crystal structure properties of photoanodes, Fig. 1a and S1a show the XRD patterns of α -Fe₂O₃, FH, unIFH and IFH photoanodes. The XRD patterns were indexed by JCPDS database. These photoanodes show similar diffraction peaks, indicating that the crystal structure of α -Fe₂O₃ is not changed by F doping and decoration of In₂S₃ NPs. Fig. S1b shows that In₂S₃ powder has obvious diffraction peak, which indicates that In₂S₃ has good crystal shape. However, the XRD patterns of unIFH and IFH photoanode does not index the characteristic diffraction peaks of In₂S₃, which may be due to the low concentration and small size characteristics [40].

Fig. S2a and b show SEM images of α -Fe₂O₃ and FH photoanodes. Subtle morphologic differences can be seen, namely, the morphology of FH nanorods array is messier than that of α -Fe₂O₃, which is attributed to F doping. In Fig. 1b and c, unIFH and IFH clearly exhibit coarser surface morphology than FH, which are preliminarily attributed to the decoration of In₂S₃ NPs. Furthermore, TEM images (Fig. S2c and d) of α -Fe₂O₃ and FH show their nanorod-like structure. Fig. 1d and f show that there are indeed external NPs attached to the surface of FH nanorods. Further, HRTEM was used to characterize the structure of these external NPs. As shown in Fig. S2e and d, α -Fe₂O₃ and FH exhibit the same lattice fringes ($d = 0.25$ nm, corresponding to the (110) crystal planes of α -Fe₂O₃), which indicates that F doping does not change the crystal structure of α -Fe₂O₃. In Fig. 1e and g, in addition to the FH nanorods showing lattice fringes of 0.249 nm, the external NPs also show clear lattice spacing

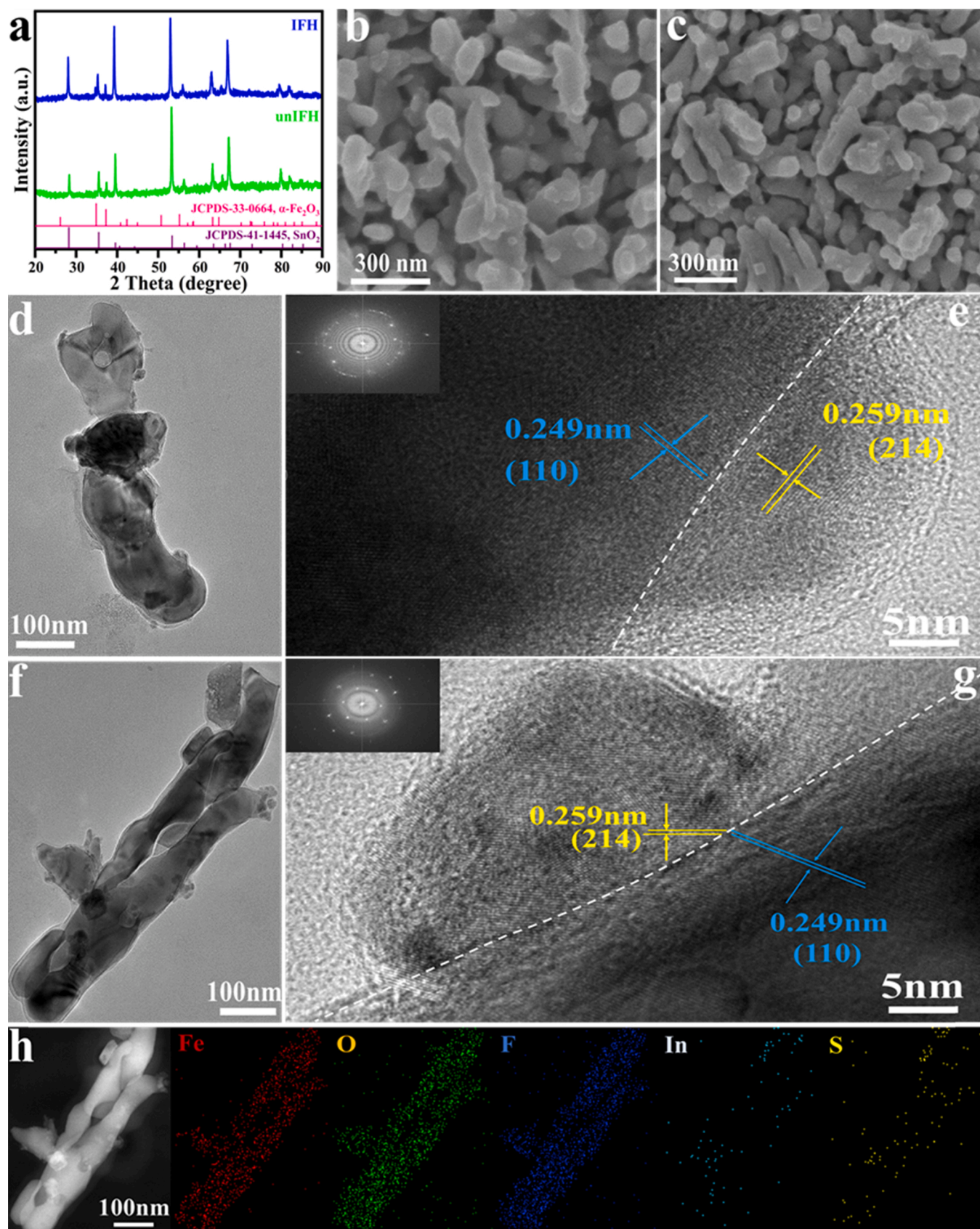


Fig. 1. (a) XRD patterns of unIFH and IFH photoanodes. SEM images of (b) unIFH and (c) IFH. TEM (d) and HRTEM (inset, FFT) (e) images of unIFH. TEM (f) and HRTEM (inset, FFT) (g), EDS elemental mapping (h) of IFH photoanode.

($d = 0.259$ nm, corresponding to the (214) crystal plane of In_2S_3). This demonstrates the successful decoration of In_2S_3 NPs. However, it is worth noting that lattice mismatch occurs at the interface of the two phases in unIFH (Fig. 1e), while the lattice of the two phases in IFH can be well matched at the interface (Fig. 1g). These indicate that In_2S_3 NPs decorated only by hydrothermal reaction and FH do not match well, but further annealing can make two phases tight and eliminate the lattice mismatch phenomenon. The Fast Fourier Transform (FFT) (inset in Fig. 1e and g) also helps to prove that IFH has a better crystallinity. In addition, the EDS elemental mapping of the IFH photoanode are shown in Fig. 1h, and it can also be seen that the uniform distribution of Fe, O and F elements and the successful decoration of In_2S_3 NPs.

In order to investigate the optical properties of all samples, the UV–vis absorption spectra of $\alpha\text{-Fe}_2\text{O}_3$, FH, unIFH, IFH photoanodes and In_2S_3 powder are shown in Fig. S3. All samples show similar light absorption range, which indicate that F doping and the decoration of In_2S_3 NPs hardly change the light absorption range of the photoanode. The band gap energy calculated for each sample based on the UV–vis absorption spectra will be discussed in the following section.

In order to further confirm the composition of IFH heterostructure and the chemical states of the elements, XPS measurements were performed on all samples. In Fig. S4a, the peaks of Fe $2p_{3/2}$ and Fe $2p_{1/2}$ can be deconvolution into two peaks, respectively, accompanied by two satellite peaks. The two peaks at 710.10 eV and 723.78 eV binding energies are allocated to Fe $2p_{3/2}$ and Fe $2p_{1/2}$, respectively, which belong to the Fe^{3+} in $\alpha\text{-Fe}_2\text{O}_3$ [51]. At the same time, FH has deconvolution

peaks similar to those of $\alpha\text{-Fe}_2\text{O}_3$, and the binding energies of Fe $2p_{3/2}$ and Fe $2p_{1/2}$ move to the higher values of 710.20 eV and 723.80 eV, respectively, which are attributed to the strong electronegativity of F to attract electrons from Fe^{3+} [51]. Further, as shown in Fig. 2a, the XPS spectrum of Fe 2p of unIFH shows deconvolution peaks at the same position as those of FH. However, for IFH, the binding energies of Fe $2p_{3/2}$ and Fe $2p_{1/2}$ move to the lower values of 710.10 eV and 723.76 eV, respectively, because electrons flow from the heterogeneous In_2S_3 to FH. As shown in Fig. 2b and S4b, $\alpha\text{-Fe}_2\text{O}_3$, FH and unIFH show similar deconvolution peaks of O 1s, and the two fitting peaks are attributed to Fe-O and adsorbed hydroxyl group, respectively [52]. Of particular note is the high-resolution XPS spectrum of O 1s of IFH, where a strong peak at 531.33 eV is assigned to the S-O bond between In_2S_3 and FH [40,49], in addition to a peak at 529.64 eV attributed to lattice oxygen (Fe-O) [53]. In Fig. S4c and d, the single peak of XPS spectra of F 1s indicates the successful doping of F [52]. Furthermore, as shown in Fig. 2c and S5a, the binding energies of In $3d_{5/2}$ (444.64 eV) and In $3d_{3/2}$ (452.18 eV) of IFH are greater than those of In $3d_{5/2}$ (444.44 eV) and In $3d_{3/2}$ (451.98 eV) of pure In_2S_3 powder; however, the peak positions of unIFH and In_2S_3 powder are almost the same. These indicate that In_2S_3 and FH in unIFH photoanode are only physical adsorption, while In_2S_3 and FH in IFH photoanode have chemical interaction, and electrons are transferred from In_2S_3 to FH [49]. In addition, Fig. 2d and S6b exhibit that unIFH has deconvolution peaks consistent with In_2S_3 powder. Compared with them, for S 2p of IFH (Fig. 2d), not only two peaks at 161.36 eV (S $2p_{3/2}$) and 162.47 eV (S

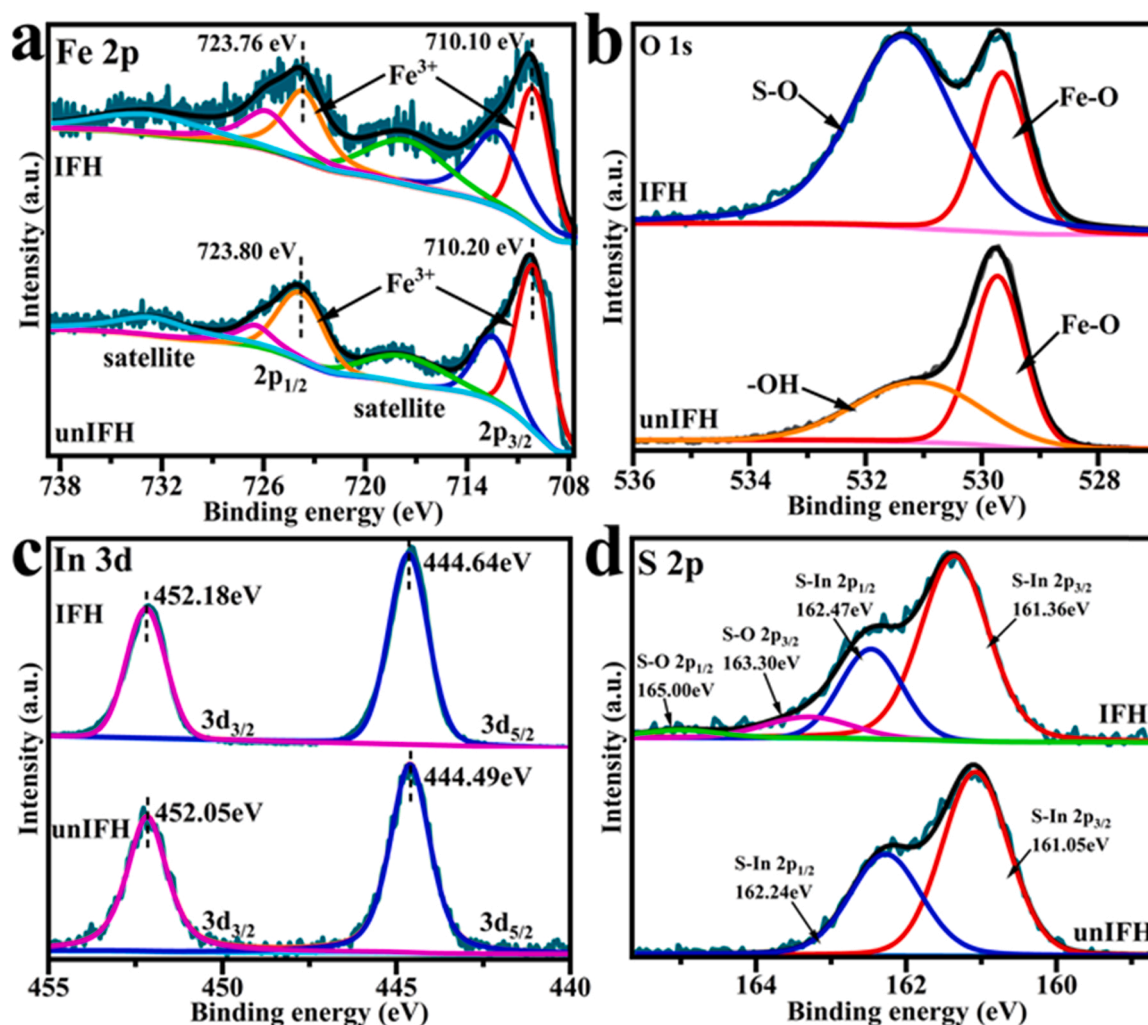


Fig. 2. XPS spectra of (a) Fe 2p, (b) O 1s, (c) In 3d and (d) S 2p of IFH and unIFH photoanodes.

$2p_{1/2}$) are observed to be assigned to S-In bond [50], but also two peaks at 163.30 eV (S $2p_{3/2}$) and 165.00 eV (S $2p_{1/2}$) are observed to be assigned to S-O bond [40]. Considering the above, it can be known that the annealing process (10 min in an atmosphere of argon at 350 °C) is responsible for the formation of S-O bond by comparing the high-resolution XPS spectra of unIFH and IFH. At the same time, the S-O bond between In_2S_3 and FH not only combines two phases, but also provides a channel for charge transfer. Accordingly, a hypothetical scheme (Scheme S2) is proposed that the matching of incompatible layers in heterostructures are usually countered by the formation of defects [40]. These defects can adversely affect charge separation and transfer within heterogeneous structures, which are usually photo-generated carrier recombination centers. The S-O chemical bond between the two phases makes heterogeneous structure more solid and reduces the surface defect states. Therefore, the formation of high-quality S-O bonds during annealing process is indispensable, and the XPS analyses above also preliminarily confirm the appropriate construction of heterojunction between In_2S_3 and FH.

3.2. Photoelectrochemical performance

As shown in Fig. 3a, $\alpha\text{-Fe}_2\text{O}_3$, FH, unIFH and IFH photoanodes obtain photocurrent densities of 0.64, 1.39, 1.27 and 2.21 mA cm^{-2} at 1.23 V_{RHE} , respectively. The photocurrent density of IFH photoanode is 3.45 times higher than that of the pristine $\alpha\text{-Fe}_2\text{O}_3$. Among them, LSV curves of IFH photoanodes in the optimization process at different concentrations and hydrothermal time are shown in Fig. S6a and b, respectively. Nevertheless, the photocurrent density of the unIFH

photoanode is much less satisfactory than that of the IFH photoanode (Fig. 3a). Correspondingly, Fig. 3b shows LSV curves of each photoanode under chopping irradiation condition. The results show that there is no current response under non-irradiation conditions, which proves that only PEC performance has been measured [49]. At the same time, the recombination degree of photogenerated carriers can be roughly known by observing the "peak" characteristics of each irradiation switch. To be specific, the "peak" of FH is weaker than that of $\alpha\text{-Fe}_2\text{O}_3$, which indicates that the recombination of photogenerated carriers can be reduced by F doping; IFH showed the weakest peak, while unIFH showed the strongest peak, suggesting that In_2S_3 NPs bonded by S-O bond can further reduce carrier recombination, while In_2S_3 NPs loaded only by physical adsorption may cause additional surface defect states, providing recombination sites for electron-hole [40]. Based on LSV results, it is easy to know that the formation of S-O chemical bond between In_2S_3 and FH is very important for the improvement of PEC performance of $\alpha\text{-Fe}_2\text{O}_3$ -based photoanode. Furthermore, the applied bias photon-to-current conversion efficiency (ABPE) was calculated from Eq. S2 in the Supporting information, and that of $\alpha\text{-Fe}_2\text{O}_3$, FH, unIFH and IFH photoanodes are 0.061%, 0.076%, 0.065% and 0.145%, respectively (Fig. 3c). Moreover, the IPCE curves were tested to study the effect of photocurrent density enhancement under incident light of different wavelengths. As shown in Fig. 3d, the IPCE of $\alpha\text{-Fe}_2\text{O}_3$, FH, unIFH and IFH at 350 nm are 9%, 21%, 15% and 35%, respectively. As described, IFH has the best energy conversion efficiency while unIFH has a poor energy conversion efficiency, which indirectly proves that S-O bond significantly improves solar energy conversion efficiency. In addition, Table S1 shows the comparison of our IFH photoanode to other

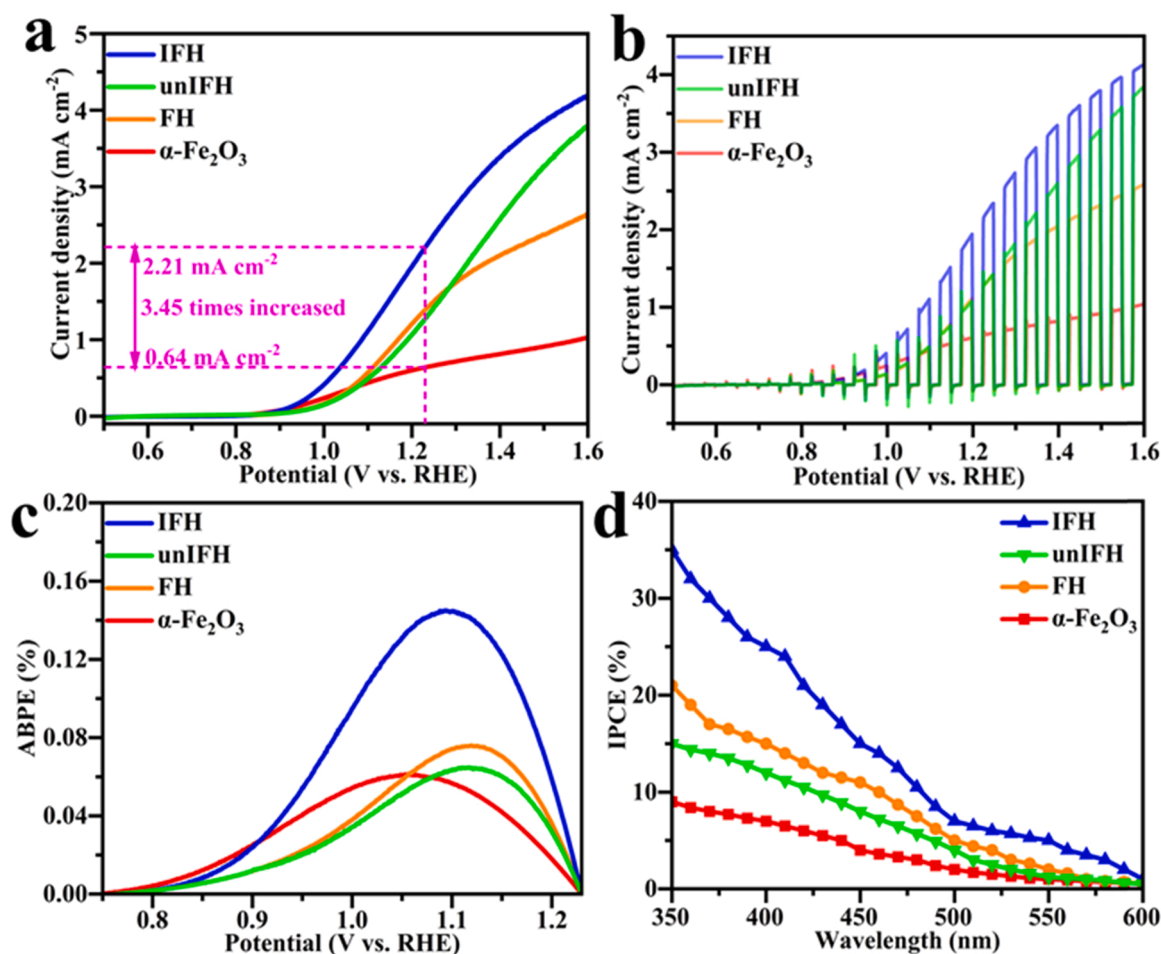


Fig. 3. Photoelectrochemical performance of $\alpha\text{-Fe}_2\text{O}_3$, FH, unIFH and IFH photoanodes. (a) Linear sweep voltammetry (LSV) curves, (b) chopped LSV scans, (c) ABPE curves and (d) IPCE curves at 1.23 V_{RHE} .

α -Fe₂O₃-based photoanodes.

In order to deeply understand the reasons for the enhanced PEC performance of the improved photoanode and the effect of S-O bond on photoanode, complete electrochemical tests and theoretical analyses were carried out. In Fig. 4a, the transient photocurrent curves were obtained to study electron-hole recombination on the photoanode surface. As shown in the dotted circle mark, compared with FH, IFH shows a smaller "sharp peak" and unIFH shows a stronger "sharp peak" at the moment when illumination turned off and switched on, which indicates that In₂S₃ NPs bonded by S-O bond could reduce the surface defect states, instead In₂S₃ NPs only decorated with physical adsorption increase the surface defect states and lead to serious carrier recombination. Further, the measurement results of open-circuit photovoltage (OCP) are shown in Fig. 4b. When the voltage difference (ΔV_{OC}) between light off and on is larger, the surface defect state is less and the band bending degree is larger. And then, the ΔV_{OC} of α -Fe₂O₃, FH, unIFH and IFH are 0.31 V_{RHE}, 0.36 V_{RHE}, 0.35 V_{RHE} and 0.56 V_{RHE}, respectively. FH exhibits increased ΔV_{OC} than the pristine α -Fe₂O₃, suggesting the reduction of surface defect states by F doping [54]. Afterwards the integration of heterogeneous In₂S₃ NPs and FH by S-O chemical bond, IFH shows a further increased ΔV_{OC} , indicating that the modification of In₂S₃ NPs with S-O bond further reduces the surface states of FH and increased the band bending degree. This can effectively inhibit surface carrier recombination, accelerate charge transfer and promote electron-hole pairs separation. Conversely, unIFH exhibits decreased ΔV_{OC} than the FH, indicating that the In₂S₃ NPs only loaded by physical adsorption could cause more surface defect states, which would be harmful to charge separation.

As shown in Fig. 4c, the positive slope in the Mott-Schottky diagram

reflects that α -Fe₂O₃ is an n-type semiconductor, F doping is an n-type semiconductor properties. The donor density (N_D) values were calculated according to Eq. S3 of the Supporting information. The results show that the N_D of FH is about one order of magnitude higher than that of pristine α -Fe₂O₃, which is attributed to the significantly increased carrier density due to the doping of functional heteroatom fluorine [51]. Moreover, the N_D of IFH is about 20 times higher than that of pristine α -Fe₂O₃, which may be due to the reduction of surface defects due to the S-O bond formed between the heterogeneous In₂S₃ NPs and FH. The flat band potentials (ϕ_{fb}) of α -Fe₂O₃, FH and IFH shift negatively in turn, indicating that the Fermi pin effect is reduced by F doping and the S-O bonded In₂S₃ heterostructure could further increase the band bending degree [54]. However, compared with FH, unIFH shows a smaller N_D and a more positive ϕ_{fb} due to the additional surface defect state caused by the physical adsorption of In₂S₃ NPs.

The electrochemical impedance spectra (EIS) were measured under the illumination of 1.23 V_{RHE} to further research the charge transfer of all photoanodes. In Fig. 4d, Nyquist plots were fitted according to the two-RC-unit equivalent circuit (embedded circuit diagram). Detailed

Table 1

The fitted resistances of α -Fe₂O₃, FH, unIFH and IFH photoanodes.

Sample	R_{trap} (Ω cm ⁻²)	R_{ct} (Ω cm ⁻²)
α -Fe ₂ O ₃	157.1	281.1
FH	68.8	93.5
unIFH	44.2	125.5
IFH	36.8	78.4

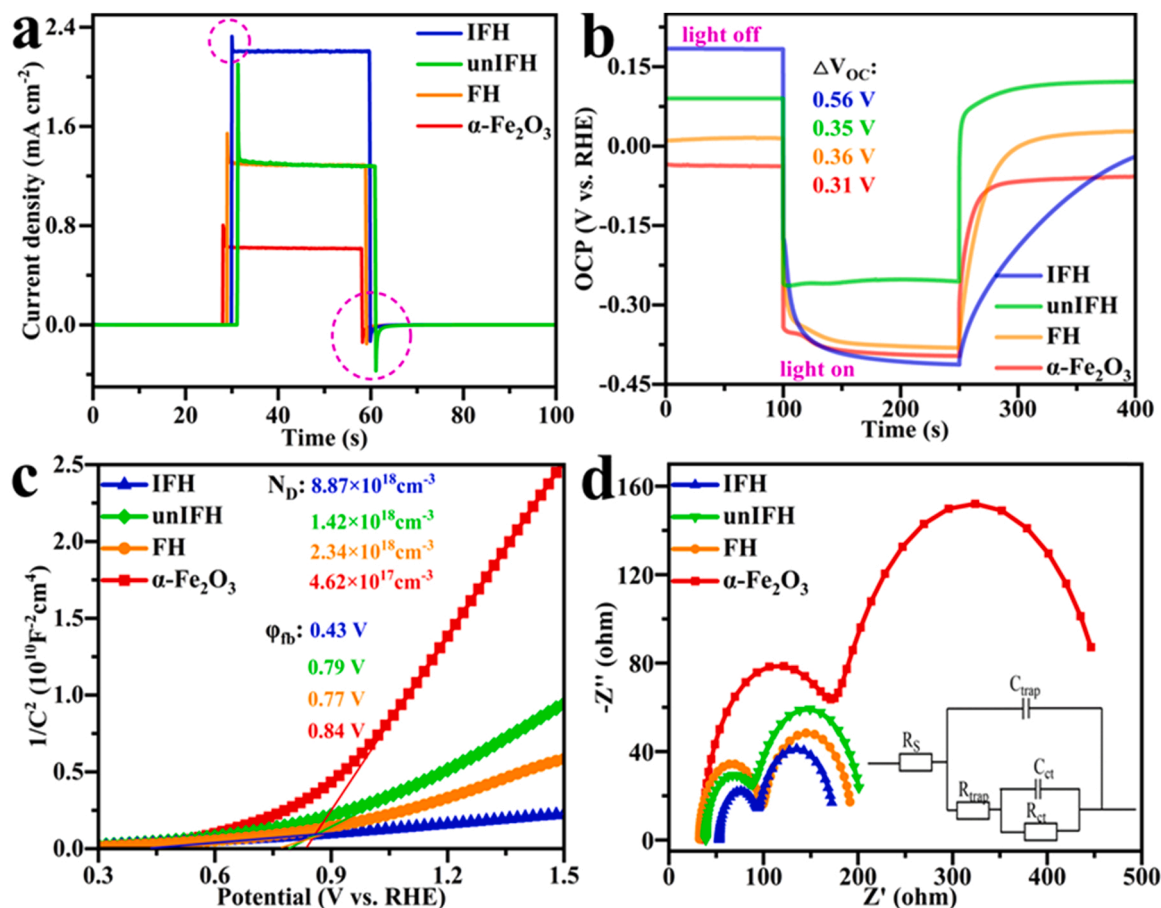


Fig. 4. (a) Transient photocurrent density curves, (b) open circuit photovoltage curves, (c) Mott-Schottky plots and (d) electrochemical impedance spectra at 1.23 V_{RHE} (the embedded diagram is an equivalent circuit diagram).

resistance values fitted for $\alpha\text{-Fe}_2\text{O}_3$, FH, unIFH and IFH photoanodes are shown in Table 1, where R_{trap} corresponds to the charge transport resistance within the bulk semiconductor and R_{ct} relates to charge transfer resistance across the interface of semiconductor and electrolyte [51]. From $\alpha\text{-Fe}_2\text{O}_3$ to FH, R_{trap} and R_{ct} decrease obviously, which are attributed to an increase in carrier concentration and a decrease in part of the surface captured states by F doping [51]. At the same time, IFH shows lower R_{trap} and R_{ct} than FH, while unIFH shows higher R_{trap} and R_{ct} than IFH, indicating that the surface state of FH was passivated and formed heterojunction with S-O bonded In_2S_3 , which are beneficial to the separation and transport of photogenerated charge. In order to evaluate the lifetime of charge carriers, fitted Bode plots based on the EIS spectra are shown in Fig. S7 [55]. The lifetime (τ) of the photogenerated charge can be calculated from Eq. S4 of the supporting information. Based on Fig. S7 and Eq. S4, the τ of $\alpha\text{-Fe}_2\text{O}_3$, FH, unIFH and IFH is 0.159 ms, 0.615 ms, 0.418 ms and 0.741 ms, respectively. It can be seen that F doping can prolong the lifetime of photogenerated charge, and S-O bonded In_2S_3 can further prolong the lifetime of photogenerated charge, while In_2S_3 NPs only adsorbed by physical adsorption may increase the surface trapped states and provide sites for electron-hole recombination.

To further clarify the source of the enhanced water oxidation activity, the electrochemical active surface area (EASA) values were obtained based on relevant calculations and voltammetry (Fig. S8) in the Supporting information. In Fig. S9, capacitance of double layer (Cdl) value of $\alpha\text{-Fe}_2\text{O}_3$, FH, unIFH and IFH is 24.6, 60.4, 45.4 and 80.9 $\mu\text{F cm}^{-2}$, respectively. These suggest that the F doping and the decoration of heterogeneous In_2S_3 NPs can provide more water oxidation active sites for the $\alpha\text{-Fe}_2\text{O}_3$ -based photoanode by reducing the surface defect states. These results indicate that F doping can improve the surface charge

distribution of $\alpha\text{-Fe}_2\text{O}_3$ [54], and S-O bonded In_2S_3 can further eliminate the surface defect states and expose water oxidation active sites, while In_2S_3 modified only by physical adsorption causes additional surface defect states and leads to the reduction of the active sites.

In order to accurately evaluate the improved photoanode's for enhancement of charge separation efficiency, the bulk phase separation efficiency (η_{bulk}) and surface injection efficiency (η_{surface}) of the electron-hole pairs were further calculated based on Eq. S5-S9. Among them, the photocurrent densities of all photoanodes were measured using 1 M Na_2SO_3 electrolyte as the hole sacrifice agent (Fig. S10). In Fig. 5a, the η_{bulk} of $\alpha\text{-Fe}_2\text{O}_3$, FH, unIFH and IFH is 12.7%, 22.2%, 21.8% and 31.0%, respectively. In Fig. 5b, the η_{surface} of $\alpha\text{-Fe}_2\text{O}_3$, FH, unIFH and IFH is 51.5%, 62.5%, 57.7% and 69.1%, respectively. It can be seen that IFH has a significantly improved η_{bulk} and η_{surface} , which are attributed to the formation of heterojunction between the FH and In_2S_3 decorated with S-O bond, thus facilitating charge separation. However, unIFH shows a lower η_{surface} than FH at 1.23 V_{RHE}, which is attributed to the additional surface defect states caused by the loading of In_2S_3 only by physical adsorption, leading to serious recombination of surface electrons and holes.

In order to evaluate the application potential of the target photoanode in PEC water splitting, the Faradaic efficiency was calculated by measuring the volume of oxygen released and comparing it with theoretical values (Fig. 5c). The experimental results of IFH are in good agreement with the theoretical values, and the average Faradaic efficiency is over 90%, indicating that the observed current and O_2 are indeed coming from PEC water oxidation reaction rather than other processes [45].

Equally important, the good long-term stability of the improved photoanode is the prerequisite for its application. Fig. 5d shows the

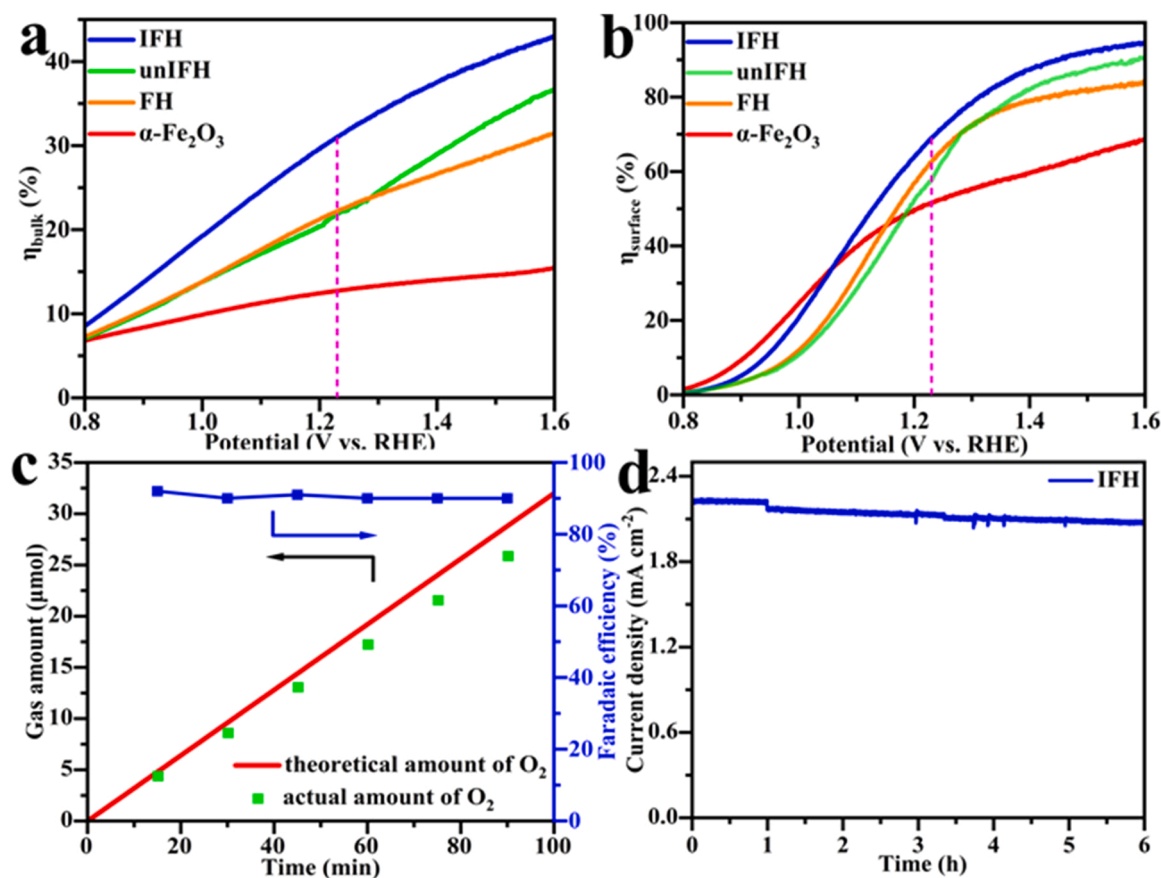


Fig. 5. (a) Bulk charge separation efficiency (η_{bulk}) and (b) surface charge injection efficiency (η_{surface}) of $\alpha\text{-Fe}_2\text{O}_3$, FH, unIFH and IFH photoanodes. (c) Amount of O_2 evolved as well as the Faradaic efficiency of IFH photoanode. (d) Chronoamperometry curves of the IFH photoanode for 6 h at 1.23 V_{RHE}.

long-term stability of the IFH photoanode. The IFH photoanode presented good stability and an acceptable attenuation of photocurrent density after 6-hour detection time. In order to explore the attenuation of current density of IFH photoanode after 6 h of long-term stability test, a series of physical characterizations were tested. The XRD pattern (Fig. S11a) of IFH photoanode after 6-hour stability test shows diffraction peaks similar to those of IFH photoanode before the test (Fig. 1a), indicating that the phase of the improved photoanode did not change after a long time of operation. SEM (Fig. S11b), TEM (Fig. S11c) and HRTEM (Fig. S11d) images of the IFH photoanode after 6-hour stability test are generally consistent with those before the test. Among them, Fig. S11d shows that the lattices of the two phases can still match well at

the heterogeneous interface. In addition, the XPS spectra (Fig. S12) of Fe 2p, F 1s, In 3d and S 2p of IFH photoanode after 6-hour stability test is similar to those of IFH photoanode before the test. It is worth noting that, compared with the IFH photoanode before the long-term stability test, the XPS spectrum of O 1s of the IFH photoanode after the test shows a decrease in the peak intensity of S-O bond (Fig. S12b). This may account for the slight attenuation of the photocurrent density after 6-hour stability test, and also indicates that the S-O bond is critical to the PEC water oxidation performance of the IFH photoanode.

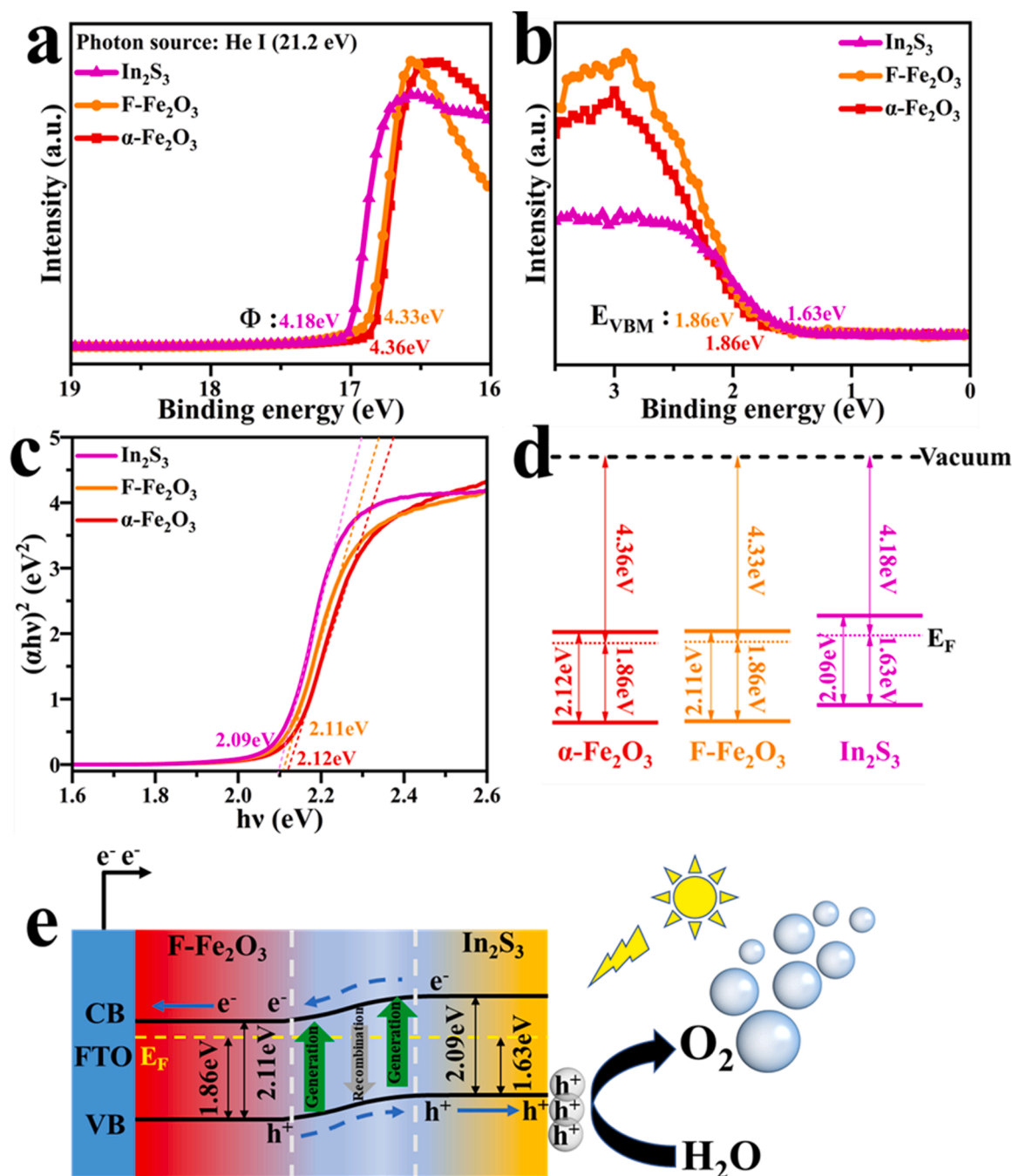


Fig. 6. Characterization of energy band position. (a) UPS, (b) XPS valence band spectroscopy and (c) calculated band gap values (based on UV-vis absorption spectra) of $\alpha\text{-Fe}_2\text{O}_3$, $\text{F-Fe}_2\text{O}_3$ and In_2S_3 . (d) Schematic diagram of band positions drawn using the obtained values. (e) Schematic diagram of the energy band structure of type-II heterojunction with $\text{F-Fe}_2\text{O}_3$, In_2S_3 and electrolyte successively bonded.

3.3. Charge migration mechanism

In order to determine the exact band positions, the work functions (Φ ; Φ represents the energy of the Fermi level relative to the vacuum level), valence bands (VB) and band gaps of α -Fe₂O₃, F-Fe₂O₃ and In₂S₃ were determined by UPS, XPS valence band spectroscopy and UV–vis spectroscopy, respectively. Based on UPS measurements (Fig. S13) and Eq. S11, the Φ of α -Fe₂O₃, F-Fe₂O₃ and In₂S₃ are 4.36, 4.33 and 4.18 eV, respectively (Fig. 6a). According to the XPS valence band measurement results in Fig. S14, the valence band maxima (E_{VBM}) of α -Fe₂O₃, F-Fe₂O₃ and In₂S₃ were obtained, respectively, and the results are summarized in Fig. 6b. In addition, according to the UV–vis absorption spectra (Fig. S3), the calculated band gap values of α -Fe₂O₃, F-Fe₂O₃ and In₂S₃ are 2.12, 2.11 and 2.09 eV, respectively (Fig. 6c). Using the values obtained from UPS, XPS valence band spectroscopy and UV–vis measurements, a schematic diagram of band locations is drawn as shown in Fig. 6d. Compared with pristine α -Fe₂O₃, the Fermi level of F-Fe₂O₃ is closer to the bottom of the conduction band (CB), which also indicates that F doping is n-type doping and results in an increase in donor concentration, which is consistent with Mott-Schottky's analysis. According to Fig. 6d, the band matching diagram as shown in Fig. 6e was drawn, which can convincingly prove that the typical type-II heterojunction formed between F-Fe₂O₃ and In₂S₃. A built-in electric field is constructed between F-Fe₂O₃ and In₂S₃ interface, which drives the rapid separation and transfer of photogenerated electron-hole pairs and effectively inhibits the recombination of electron-hole pairs. The VB deviation between F-Fe₂O₃ and In₂S₃ provides a large driving force for the photogenerated holes, which makes the holes quickly migrate to the interface to participate in water oxidation, effectively prolonging the carrier life [49]. To be specific, the electron-hole migration mechanism of the In₂S₃/F-Fe₂O₃ photoanode is shown in Fig. 6e. The bands of F-Fe₂O₃ and In₂S₃ are bent in contact until the Fermi level is equilibrated to form a type-II heterojunction. When exposed to sunlight, photogenerated electrons are excited from VB to CB of F-Fe₂O₃ and In₂S₃. Moreover, due to different energy levels, the electrons in CB of In₂S₃ are transferred to the CB of F-Fe₂O₃ by electrostatic action, and then pass through FTO and external circuit to Pt electrode to participate in hydrogen evolution reaction. The holes in the VB of F-Fe₂O₃ transfer to the VB of In₂S₃, and then migrate to the interface between the semiconductor and electrolyte to participate in OER.

4. Conclusions

In summary, In₂S₃/F-Fe₂O₃ type-II heterostructure photoanode was prepared by two hydrothermal and annealing processes for efficient water oxidation. Without the aid of any cocatalyst, the In₂S₃/F-Fe₂O₃ photoanode exhibits content PEC performance. In addition, detailed characterizations reveal the importance of S-O bond for the system and prove the successful construction of the type-II heterojunction between F-Fe₂O₃ and In₂S₃. The built-in electric field between F-Fe₂O₃ and In₂S₃ provides a large driving force for the rapid migration of photogenerated charges, which effectively inhibits the recombination of electron hole pairs and prolongs the carrier life. Furthermore, both F doping and In₂S₃ decorated with S-O bond can greatly improve the conductivity of α -Fe₂O₃. These efforts together result in competitive current density and charge separation efficiency of In₂S₃/F-Fe₂O₃. Moreover, because In₂S₃ has a suitable band gap, it may form the desired heterojunction with some other photoanode materials, which provides an idea for the design and construction of multicomponent electrodes for PEC water splitting in the future.

CRediT authorship contribution statement

Huan Chai: Conceptualization, Methodology, Data curation, Investigation, Visualization, Writing – original draft. **Lili Gao:** Investigation. **Peng Wang:** Investigation. **Feng Li:** Funding acquisition. **Guowen Hu:**

SEM. **Jun Jin:** Funding acquisition, Supervision, Review.

Declaration of Competing Interest

The authors declare that they have no known competing financial interests or personal relationships that could have appeared to influence the work reported in this paper.

Acknowledgments

This work is financially supported by the Natural Science Foundation of Gansu (21JR7RA474), the Key Laboratory of Catalytic Engineering of Gansu Province and Resources Utilization, Gansu Province for financial support, the Foundation of State Key Laboratory of High-efficiency Utilization of Coal and Green Chemical Engineering (Grant No. 2021-K57), the Natural Science Foundation of Ningxia Hui Autonomous Region (2020AAC03017), the Natural Science Foundation for Excellent Youth Scholars of Ningxia Hui Autonomous Region (2021AAC05002), the National Natural Science Foundation of China (21908115, 22108131).

Appendix A. Supporting information

Supplementary data associated with this article can be found in the online version at doi:10.1016/j.apcatb.2021.121011.

References

- [1] T. Hisatomi, J. Kubota, K. Domen, Recent advances in semiconductors for photocatalytic and photoelectrochemical water splitting, *Chem. Soc. Rev.* 43 (2014) 7520–7535, <https://doi.org/10.1039/C3CS60378D>.
- [2] K. Sivula, R. van de Krol, Semiconducting materials for photoelectrochemical energy conversion, *Nat. Rev. Mater.* 1 (2016), <https://doi.org/10.1038/natrevmats.2015.10> (15010).
- [3] C. Li, Z. Luo, T. Wang, J. Gong, Surface, bulk, and interface: rational design of hematite architecture toward efficient photo-electrochemical water splitting, *Adv. Mater.* 30 (2018), 1707502, <https://doi.org/10.1002/adma.201707502>.
- [4] X. Ning, D. Yin, Y. Fan, Q. Zhang, P. Du, D. Zhang, J. Chen, X. Lu, Plasmon-enhanced charge separation and surface reactions based on Ag-loaded transition-metal hydroxide for photoelectrochemical water oxidation, *Adv. Energy Mater.* 11 (2021), 2100405, <https://doi.org/10.1002/aenm.202100405>.
- [5] K.C. Kwon, S. Choi, K. Hong, C.W. Moon, Y.-S. Shim, D.H. Kim, T. Kim, W. Sohn, J.-M. Jeon, C.-H. Lee, K.T. Nam, S. Han, S.Y. Kim, H.W. Jang, Wafer-scale transferable molybdenum disulfide thin-film catalysts for photoelectrochemical hydrogen production, *Energy Environ. Sci.* 9 (2016) 2240–2248, <https://doi.org/10.1039/C6EE00144K>.
- [6] A. Duret, M. Grätzel, Visible light-induced water oxidation on mesoscopic α -Fe₂O₃ films made by ultrasonic spray pyrolysis, *J. Phys. Chem. B* 109 (2005) 17184–17191, <https://doi.org/10.1021/jp044127c>.
- [7] X. Cheng, G. Dong, Y. Zhang, C. Feng, Y. Bi, Dual-bonding interactions between MnO₂ cocatalyst and TiO₂ photoanodes for efficient solar water splitting, *Appl. Catal. B: Environ.* 267 (2020), 118723, <https://doi.org/10.1016/j.apcatb.2020.118723>.
- [8] P. Dias, A. Vilanova, T. Lopes, L. Andrade, A. Mendes, Extremely stable bare hematite photoanode for solar water splitting, *Nano Energy* 23 (2016) 70–79, <https://doi.org/10.1016/j.nanoen.2016.03.008>.
- [9] R.A. Gurudayal, P.P. John, C. Boix, C. Yi, M.C. Shi, S.A. Scott, A.M. Veldhuis, S. M. Minor, L.H. Zakeeruddin, M. Wong, N. Grätzel, Mathews, Atomically altered hematite for highly efficient perovskite tandem water-splitting devices, *ChemSusChem* 10 (2017) 2449–2456, <https://doi.org/10.1002/cssc.201700159>.
- [10] H. Dotan, K. Sivula, M. Grätzel, A. Rothschild, S.C. Warren, Probing the photoelectrochemical properties of hematite (α -Fe₂O₃) electrodes using hydrogen peroxide as a hole scavenger, *Energy Environ. Sci.* 4 (2011) 958–964, <https://doi.org/10.1039/C0EE00570C>.
- [11] G. Liu, N. Li, Y. Zhao, M. Wang, R. Yao, F. Zhao, Y. Wu, J. Li, Porous versus compact hematite nanorod photoanode for high-performance photoelectrochemical water oxidation, *ACS Sustain. Chem. Eng.* 7 (2019) 11377–11385, <https://doi.org/10.1021/acssuschemeng.9b01045>.
- [12] P. Peerakiatkhajohn, J.-H. Yun, H. Chen, M. Lyu, T. Butburee, L. Wang, Stable hematite nanosheet photoanodes for enhanced photoelectrochemical water splitting, *Adv. Mater.* 28 (2016) 6405–6410, <https://doi.org/10.1002/adma.201601525>.
- [13] L. Wang, J. Zhu, X. Liu, Oxygen-vacancy-dominated cocatalyst/hematite interface for boosting solar water splitting, *ACS Appl. Mater. Interfaces* 11 (2019) 22272–22277, <https://doi.org/10.1021/acsami.9b03789>.
- [14] S.L. Shinde, S. Ishii, T.D. Dao, R.P. Sugavaneshwar, T. Takei, K.K. Nanda, T. Nagao, Enhanced solar light absorption and photoelectrochemical conversion using TiN

- nanoparticle-incorporated C3N4-C dot sheets, *ACS Appl. Mater. Interfaces* 10 (2018) 2460–2468, <https://doi.org/10.1021/acsami.7b15066>.
- [15] S. Tang, W. Qiu, S. Xiao, Y. Tong, S. Yang, Harnessing hierarchical architectures to trap light for efficient photoelectrochemical cells, *Energy Environ. Sci.* 13 (2020) 660–684, <https://doi.org/10.1039/C9EE02986A>.
 - [16] Y. Zhang, H. Lv, Z. Zhang, L. Wang, X. Wu, H. Xu, Stable unbiased photoelectrochemical overall water splitting exceeding 3% efficiency via covalent triazine framework/metal oxide hybrid photoelectrodes, *Adv. Mater.* 33 (2021), 2008264, <https://doi.org/10.1002/adma.202008264>.
 - [17] Y. Kuang, T. Yamada, K. Domen, Surface and interface engineering for photoelectrochemical water oxidation, *Joule* 1 (2017) 290–305, <https://doi.org/10.1016/j.joule.2017.08.004>.
 - [18] J. Prakash, U. Prasad, X. Shi, X. Peng, B. Azeredo, A.M. Kannan, Photoelectrochemical water splitting using lithium doped bismuth vanadate photoanode with near-complete bulk charge separation, *J. Power Sources* 448 (2020), 227418, <https://doi.org/10.1016/j.jpowsour.2019.227418>.
 - [19] X. Sheng, T. Xu, X. Feng, Rational design of photoelectrodes with rapid charge transport for photoelectrochemical applications, *Adv. Mater.* 31 (2019), 1805132, <https://doi.org/10.1002/adma.201805132>.
 - [20] S.-S. Yi, B.-R. Wulan, J.-M. Yan, Q. Jiang, Highly efficient photoelectrochemical water splitting: surface modification of cobalt-phosphate-loaded Co₃O₄/Fe₂O₃ p-n heterojunction nanorod arrays, *Adv. Funct. Mater.* 29 (2019), 1801902, <https://doi.org/10.1002/adfm.201801902>.
 - [21] M. Barroso, A.J. Cowan, S.R. Pendlebury, M. Grätzel, D.R. Klug, J.R. Durrant, The role of cobalt phosphate in enhancing the photocatalytic activity of α -Fe₂O₃ toward water oxidation, *J. Am. Chem. Soc.* 133 (2011) 14868–14871, <https://doi.org/10.1021/ja205325v>.
 - [22] J. Fester, A. Makoveev, D. Grumelli, R. Gutzler, Z. Sun, J. Rodríguez-Fernández, K. Kern, J.V. Lauritsen, The structure of the cobalt oxide/Au catalyst interface in electrochemical water splitting, *Angew. Chem. Int. Ed.* 57 (2018) 11893–11897, <https://doi.org/10.1002/anie.201804417>.
 - [23] S. Niu, X.-P. Kong, S. Li, Y. Zhang, J. Wu, W. Zhao, P. Xu, Low Ru loading RuO₂/(Co,Mn)Co₃O₄ nanocomposite with modulated electronic structure for efficient oxygen evolution reaction in acid, *Appl. Catal. B: Environ.* 297 (2021), 120442, <https://doi.org/10.1016/j.apcatb.2021.120442>.
 - [24] E.-J. Kim, J. Shin, J. Bak, S.J. Lee, Kh Kim, D. Song, J. Roh, Y. Lee, H. Kim, K.-S. Lee, E. Cho, Stabilizing role of Mo in TiO₂-MoO_x supported Ir catalyst toward oxygen evolution reaction, *Appl. Catal. B: Environ.* 280 (2021), 119433, <https://doi.org/10.1016/j.apcatb.2020.119433>.
 - [25] X. Zou, A. Goswami, T. Asefa, Efficient noble metal-free (electro)catalysis of water and alcohol oxidations by zinc-cobalt layered double hydroxide, *J. Am. Chem. Soc.* 135 (2013) 17242–17245, <https://doi.org/10.1021/ja407174u>.
 - [26] L. Luo, Z.-J. Wang, X. Xiang, D. Yan, J. Ye, Selective activation of benzyl alcohol coupled with photoelectrochemical water oxidation via a radical relay strategy, *ACS Catal.* 10 (2020) 4906–4913, <https://doi.org/10.1021/acscatal.0c00660>.
 - [27] R. Gao, D. Yan, Recent development of Ni/Fe-based micro/nanostructures toward photoelectrochemical water oxidation, *Adv. Energy Mater.* 10 (2020), 1900954, <https://doi.org/10.1002/aenm.201900954>.
 - [28] P. Liao, M.C. Toroker, E.A. Carter, Electron transport in pure and doped hematite, *Nano Lett.* 11 (2011) 1775–1781, <https://doi.org/10.1021/nl200356n>.
 - [29] J.H. Seo, K. Choi, J. Nam, H. Lee, J.H. Lee, Synergetic donor-donor codoping strategy for enhanced photoelectrochemical activity of hematite, *Appl. Catal. B: Environ.* 260 (2020), 118186, <https://doi.org/10.1016/j.apcatb.2019.118186>.
 - [30] M. Li, Y. Yang, Y. Ling, W. Qiu, F. Wang, T. Liu, Y. Song, X. Liu, P. Fang, Y. Tong, Y. Li, Morphology and doping engineering of Sn-doped hematite nanowire photoanodes, *Nano Lett.* 17 (2017) 2490–2495, <https://doi.org/10.1021/acs.nanolett.7b00184>.
 - [31] D. Chen, Z. Liu, Dual-axial gradient doping (Zr and Sn) on hematite for promoting charge separation in photoelectrochemical water splitting, *ChemSusChem* 11 (2018) 3438–3448, <https://doi.org/10.1002/cssc.201801614>.
 - [32] R. Franking, L. Li, M.A. Lukowski, F. Meng, Y. Tan, R.J. Hamers, S. Jin, Facile post-growth doping of nanostructured hematite photoanodes for enhanced photoelectrochemical water oxidation, *Energy Environ. Sci.* 6 (2013) 500–512, <https://doi.org/10.1039/C2EE23837C>.
 - [33] J. Wang, J. Yang, Z. Zheng, T. Lu, W. Gao, The role of thin NiPi film for enhancing solar water splitting performance of Ti doped hematite, *Appl. Catal. B: Environ.* 218 (2017) 277–286, <https://doi.org/10.1016/j.apcatb.2017.06.042>.
 - [34] K.-Y. Yoon, J. Park, M. Jung, S.-G. Ji, H. Lee, J.H. Seo, M.-J. Kwak, S. Il Seok, J. H. Lee, J.-H. Jang, NiFeO_x decorated Ge-hematite/perovskite for an efficient water splitting system, *Nat. Commun.* 12 (2021), <https://doi.org/10.1038/s41467-021-24428-7> (4309).
 - [35] Z. Zhou, R. Zong, O.V. Prezhdo, Why silicon doping accelerates electron polaron diffusion in hematite, *J. Am. Chem. Soc.* 141 (2019) 20222–20233, <https://doi.org/10.1021/jacs.9b10109>.
 - [36] T.K. Sahu, M.K. Mohanta, M. Qureshi, Modulating water oxidation kinetics utilizing h-BN quantum dots as an efficient hole extractor on fluorine doped hematite photoanode, *J. Power Sources* 445 (2020), 227341, <https://doi.org/10.1016/j.jpowsour.2019.227341>.
 - [37] J. Xie, W. Liu, J. Xin, F. Lei, L. Gao, H. Qu, X. Zhang, Y. Xie, Dual effect in fluorine-doped hematite nanocrystals for efficient water oxidation, *ChemSusChem* 10 (2017) 4465–4471, <https://doi.org/10.1002/cssc.201701074>.
 - [38] H. Chai, P. Wang, T. Wang, L. Gao, F. Li, J. Jin, Surface reconstruction of cobalt species on amorphous cobalt silicate-coated fluorine-doped hematite for efficient photoelectrochemical water oxidation, *ACS Appl. Mater. Interfaces* 13 (2021) 47572–47580, <https://doi.org/10.1021/acsami.1c12597>.
 - [39] Y. Hou, F. Zuo, A. Dagg, P. Feng, A three-dimensional branched cobalt-doped α -Fe₂O₃ nanorod/MgFe₂O₄ heterojunction array as a flexible photoanode for efficient photoelectrochemical water oxidation, *Angew. Chem. Int. Ed.* 52 (2013) 1248–1252, <https://doi.org/10.1002/anie.201207578>.
 - [40] Y. Zhang, Y. Huang, S.-S. Zhu, Y.-Y. Liu, X. Zhang, J.-J. Wang, A. Braun, Covalent S-O bonding enables enhanced photoelectrochemical performance of Cu₂S/Fe₂O₃ heterojunction for water splitting, *Small* 17 (2021), 2100320, <https://doi.org/10.1002/anie.201207578>.
 - [41] J. Ma, Q. Wang, L. Li, X. Zong, H. Sun, R. Tao, X. Fan, Fe₂O₃ nanorods/CuO nanoparticles p-n heterojunction photoanode: effective charge separation and enhanced photoelectrochemical properties, *J. Colloid Interface Sci.* 602 (2021) 32–42, <https://doi.org/10.1016/j.jcis.2021.05.140>.
 - [42] F. Li, J. Li, J. Zhang, L. Gao, X. Long, Y. Hu, S. Li, J. Jin, J. Ma, NiO nanoparticles anchored on phosphorus-doped α -Fe₂O₃ nanoarrays: an efficient hole extraction p-n heterojunction photoanode for water oxidation, *ChemSusChem* 11 (2018) 2156–2164, <https://doi.org/10.1002/cssc.201800571>.
 - [43] S.-S. Yi, Z.-Y. Wang, H.-M. Li, Z. Zafar, Z.-T. Zhang, L.-Y. Zhang, D.-L. Chen, Z.-Y. Liu, X.-Z. Yue, Coupling effects of indium oxide layer on hematite enabling efficient photoelectrochemical water splitting, *Appl. Catal. B: Environ.* 283 (2021), 119649, <https://doi.org/10.1016/j.apcatb.2020.119649>.
 - [44] J. Deng, Q. Zhuo, X. Lv, Hierarchical TiO₂/Fe₂O₃ heterojunction photoanode for improved photoelectrochemical water oxidation, *J. Electroanal. Chem.* 835 (2019) 287–292, <https://doi.org/10.1016/j.jelechem.2019.01.056>.
 - [45] Z. Masoumi, M. Tayebi, M. Kolaei, A. Tayyebi, H. Ryu, J.I. Jang, B.-K. Lee, Simultaneous enhancement of charge separation and hole transportation in a W: α -Fe₂O₃/MoS₂ photoanode: a collaborative approach of MoS₂ as a heterojunction and W as a metal dopant, *ACS Appl. Mater. Interfaces* 13 (2021) 39215–39229, <https://doi.org/10.1021/acsami.1c08139>.
 - [46] Q. Peng, J. Wang, Z. Feng, C. Du, Y. Wen, B. Shan, R. Chen, Enhanced photoelectrochemical water oxidation by fabrication of p-LaFeO₃/n-Fe₂O₃ heterojunction on hematite nanorods, *J. Phys. Chem. C* 121 (2017) 12991–12998, <https://doi.org/10.1021/acs.jpcc.7b01817>.
 - [47] M.G. Ahmed, T.A. Kandiel, A.Y. Ahmed, I. Kretschmer, F. Rashwan, D. Bahnemann, Enhanced photoelectrochemical water oxidation on nanostructured hematite photoanodes via p-CaFe₂O₄/n-Fe₂O₃ heterojunction formation, *J. Phys. Chem. C* 119 (2015) 5864–5871, <https://doi.org/10.1021/jp512804p>.
 - [48] H. Zhang, Y.K. Kim, H.Y. Jeong, J.S. Lee, A few atomic FeNbO₄ overlayers on hematite nanorods: microwave-induced high temperature phase for efficient photoelectrochemical water splitting, *ACS Catal.* 9 (2019) 1289–1297, <https://doi.org/10.1021/acscatal.8b04034>.
 - [49] J. Park, T.H. Lee, C. Kim, S.A. Lee, M.-J. Choi, H. Kim, J.W. Yang, J. Lim, H. W. Jang, Hydrothermally obtained type-II heterojunction nanostructures of In₂S₃/TiO₂ for remarkably enhanced photoelectrochemical water splitting, *Appl. Catal. B: Environ.* 295 (2021), 120276, <https://doi.org/10.1016/j.apcatb.2021.120276>.
 - [50] W. Tian, C. Chen, L. Meng, W. Xu, F. Cao, L. Li, PVP treatment induced gradient oxygen doping in In₂S₃ nanosheet to boost solar water oxidation of WO₃ nanorod array photoanode, *Adv. Energy Mater.* 10 (2020), 1903951, <https://doi.org/10.1002/aenm.201903951>.
 - [51] T. Wang, X. Long, S. Wei, P. Wang, C. Wang, J. Jin, G. Hu, Boosting hole transfer in the fluorine-doped hematite photoanode by depositing ultrathin amorphous FeOOH/CoOOH cocatalysts, *ACS Appl. Mater. Interfaces* 12 (2020) 49705–49712, <https://doi.org/10.1021/acsami.0c15568>.
 - [52] C. Wang, X. Long, S. Wei, T. Wang, F. Li, L. Gao, Y. Hu, S. Li, J. Jin, Conformally coupling CoAl-layered double hydroxides on fluorine-doped hematite: surface and bulk co-modification for enhanced photoelectrochemical water oxidation, *ACS Appl. Mater. Interfaces* 11 (2019) 29799–29806, <https://doi.org/10.1021/acsami.9b07417>.
 - [53] S. Zhang, Z. Liu, D. Chen, W. Yan, An efficient hole transfer pathway on hematite integrated by ultrathin Al₂O₃ interlayer and novel CuCoO_x cocatalyst for efficient photoelectrochemical water oxidation, *Appl. Catal. B: Environ.* 277 (2020), 119197, <https://doi.org/10.1016/j.apcatb.2020.119197>.
 - [54] F. Li, J. Li, L. Gao, Y. Hu, X. Long, S. Wei, C. Wang, J. Jin, J. Ma, Construction of an efficient hole migration pathway on hematite for efficient photoelectrochemical water oxidation, *J. Mater. Chem. A* 6 (2018) 23478–23485, <https://doi.org/10.1039/C8TA07832G>.
 - [55] A.E.A. Bakr, W.M.A. El Rouby, M.D. Khan, A.A. Farghali, B. Xulu, N. Revaprasadu, Synthesis and characterization of Z-scheme α -Fe₂O₃ NTs/ruptured tubular g-C₃N₄ for enhanced photoelectrochemical water oxidation, *Sol. Energy* 193 (2019) 403–412, <https://doi.org/10.1016/j.solener.2019.09.052>.